Оптический журнал

Оптическое приборостроение

УДК 535.8; 004.27; 537.5

Электрооптический модулятор направленной связи на основе поверхностных плазмон-поляритонов для кольцевых оптических сетей на кристалле

© 2020 г. Liang Zhi-Xun, Xu Chuan-Pei, Zhu Ai-Jun, Hu Cong, Du She-Hui, Zhao Chun-Xia

Электрооптические модуляторы являются ключевыми компонентами оптических сетей на кристалле. Разработан электрооптический модулятор направленной связи на основе поверхностных плазмон-поляритонов, позволяющий избавиться от таких недостатков, характерных для традиционных электрооптических устройств (например, кольцевых микрорезонаторов), как значительные площади опорных поверхностей, низкая термическая стабильность и невысокие частоты модуляции. Построена теория его работы на основе метода связанных мод. Модулятор обеспечивает управление изменением концентрации носителей в материале, активированном оксидом индия-олова, путем подачи электрического напряжения, что приводит к изменению коэффициента преломления в пленке. Для анализа передачи сигнала от модулятора в оптическую сеть на кристалле используется теория связанных мод. Данный тип модулятора подходит для оптических сетей на кристалле с кольцевой топологией. Для моделирования и анализа использована трехмерная схема конечных разностей во временной области, исследованы оптимизационные параметры структуры. Показана работа устройства на длине волны 1550 нм с эффективностью связи более 90%, потерями на вводе 1,17 дБ, коэффициентом экстинкции 15,4 дБ, при частоте модуляции до 0,75 Тбит/с. Габариты устройства 3,8×3,2×1,2 мкм.

Результаты работы предоставляют теоретический базис для конструирования электрооптических модуляторов для направленной связи на основе поверхностных плазмон-поляритонов для применения в кольцевых оптических сетях на кристалле.

Ключевые слова: *электрооптический модулятор, поверхностные плазмон-поляритоны, кольцевые оптические сети на кристалле, оксид индия-олова, метод конечных разностей во временной области, кремниевая фотоника*

Directional coupling surface plasmon polaritons electro-optic modulator for optical ring networks-on-chip

© 2020 Liang Zhi-Xun*, **, ***, Xu Chuan-Pei*, ***, Zhu Ai-Jun*, ***, Hu Cong*, ***, Du She-Hui*, ***, Zhao Chun-Xia*, ***

*School of Electronic Engineering and Automation, Guilin University of Electronic Technology, Guilin, Guangxi, China
**School of Computer and Information Engineering, Hechi University, Yizhou, Guangxi, China
***Guangxi Key Laboratory of Automatic Detecting Technology and Instruments, Guilin, Guangxi, China

E-mail: xcp@guet.edu.cn

Submitted 20.04.2020

DOI:10.17586/1023-5086-2020-87-09-54-69

Electro-optic modulators are essential components of the optical network-on-chip. To resolve the large footprints, poor thermal stability, and low modulation rate of traditional optoelectronic devices such as micro-ring resonators, a directional coupled electro-optic modulator based on surface plasmon polaritons and coupled mode theory is designed. The modulator controls the change in carrier concentration of indium tin oxide activated material film by applying a voltage to realize electro-optic control. The modulator uses coupled-mode theory to couple the modulated optical signal into a ring waveguide. This type of modulator is suitable for an optical-on-chip network with an optical ring network-on-chip topology. The results show that the device operates at 1550 nm wavelength with a coupling efficiency of more than 90%, the insertion loss is 1.17 dB, the extinction ratio is 15.4 dB, the modulation rate is up to 0.75 Tbit/s, and the size is only 3.8×3.2×1.2 μm.

Keywords: *electro-optic modulator, surface plasmon polariton, optical ring network-on-chip, indium tin oxide, finite difference time domain, silicon photonics.*

OCIS codes: *230.4110, 240.6680*

INTRODUCTION

With the increasing number of integrated cores on a single chip, network-on-chip has become the key technology of next-generation multicore and many-core processor on-chip interconnections [1]. Intercore network interconnections are used to exchange data with each other, with the total communication capacity being improved [2] and the delay and clock synchronization problems of the bus structure being effectively solved. However, on-chip electrical interconnections still have the problems of large energy consumption, limited bandwidth, serious electromagnetic interference, communication delays and crosstalk. With the improvement of on-chip silicon-based optoelectronic technology, more optoelectronic devices can be integrated on-chip, and the introduction of optical on-chip networks [3] effectively solves the above problems. Several optical network-on-chip topologies have been proposed, such as the mesh, torus, and octagon topologies and their 3D equivalents. These structures have great advantages over the use of thousands of core processors. However, in the case of a large communication data volume and high real-time performance, these topologies cannot successfully meet the requirements in the case of routing reservation and forwarding. As shown in Fig. 1, Sébastien Le Beux first proposed an optical on-chip network with the optical ring network-on-chip (ORNoC) topology [4]. Based on this network, Cerutti et al. [5] and Wang et al. [6] proposed multi-ring and 3D ring structures [7]. Because the topology structure does not require route forwarding, multiple routers are not involved in the repeated unpacking of the forwarded data, and the route forwarding time is reduced, which can satisfactorily address the case of a large amount of communication between cores and high real-time re-

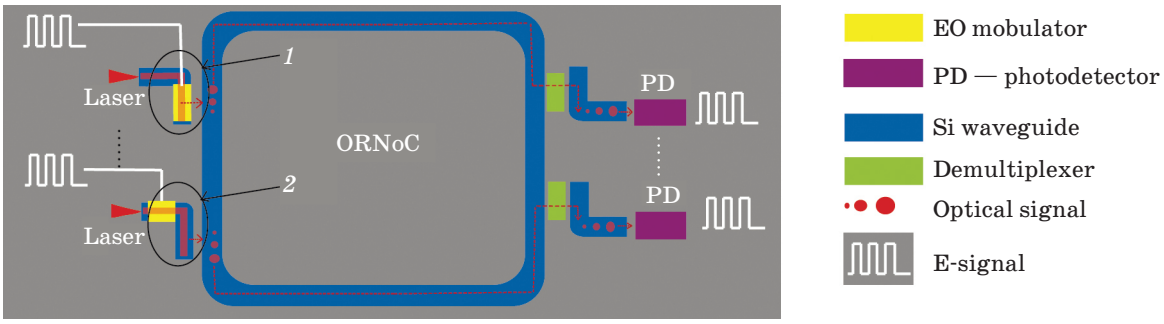

Fig. 1. An optical ring network-on-chip topology diagram and its communication framework. The network-on-chip communication mode of the ORNoC topology and two ways to realize the EOM are shown. One is to set the modulation region in the coupling area named *1*, and the other is to set the modulation area outside the coupling area named *2*.

quirements. The modulator is one of the most critical devices on the optical network-on-chip (ONoC), and scholars have performed much related research work. Micro-ring resonators and Mach-Zehnder electro-optic modulators are the current main modulation types. The size of the Mach-Zehnder electro-optic modulator (EOM) and micro-ring resonator EOM [8, 9] is usually tens of microns, and the modulation rate is generally tens of gigahertz. The micro-ring resonator modulator can be made smaller in size, but its refractive index is easily affected by temperature and poor thermal stability [10, 11]. In recent years, a large number of scholars have been drawn to the study of surface plasmon polaritons (SPP) devices, and some SPP EOMs have been designed by using indium tin oxide (ITO) activated materials [12, 13]. Badr et al. [12] proposed a plasma ultrafast EOM based on directional coupling technology, with a modulation rate up to 1 Tbit/s, an extinction ratio (ER) of 9.14 dB, and an insertion loss (IL) of less than 1 dB. Kuang et al. [14] proposed a dual-slot EOM based on epsilon-near-zero oxide, which achieves a lower IL and higher modulation efficiency of 0.37 and 14.4 dB respectively, at a wavelength of 1550 nm. Tahersimaa et al. [13] used a dual ITO-activated material film to achieve an enhanced high-speed EOM, with a modulation efficiency of 0.5 dB/μm and an IL of 2 dB. The above EOMs perform well according to the experimental results; however, the electro-optic modulation structures designed above are all straight-through EOMs, which do not take into account the network application on an optical chip similar to the ORNoC topology. This kind of EOM cannot be well applied in optical chip networks with ORNoC topologies. Therefore, in this paper, a plasma EOM with a coupling structure is proposed, and the voltage control method is improved. After adding a new electrode, the modulation rate of the device is effectively improved, and the structure is made suitable for the optical network-on-chip, such as the ORNoC topology. The modulation rate of the EOM is further improved by improving the electrode. As shown in Fig. 1, the modulator can be designed with two types of arrangements (*1* and *2* in the figure): one is to set the modulation region in the coupling area, and the other is to set the modulation area outside the coupling area. According to equation (14) below, we know that coupling can occur only when the mismatch factors are close to matching, that is, when $\delta = 0$. However, because the modulation area of this type of modulator (identified as *1* in Fig. 1) is set in the coupling area, it is difficult to achieve a mismatch factor $\delta = 0$, resulting in a low coupling efficiency of the device, which seriously increases its insertion loss. It is also proved in the simulation experiment that it is difficult to achieve a mismatch factor δ of zero. Therefore, this paper focuses on the modulator identified as *2* in Fig. 1.

In this paper, the EOM is discussed in the following four sections. First, the EOM is designed from the structure model. Then, we analyze and simulate the coupled mode theory and the electrical regulation principle of transparent conducting oxide (TCOS) with a dielectric constant. Next, we use a 3D finite difference time domain (FDTD) simulation software to optimize the parameters of the device structure model and obtain the optimal structure model parameters for simulation. Finally, we analyze the performance parameters of the designed electro-optic modulation and compare them with the device parameters proposed by scholars in recent years. The detailed design and analysis are described below.

MODEL STRUCTURAL DESIGN AND THEORETICAL ANALYSIS

Device model structural design

The device model structure designed in this paper is shown in Figs. 2a, b. It has two silicon waveguides with a refractive index of 3.48 on a low SiO_2-base with a refractive index of 1.44. One of the waveguides is used for the input and modulation of optical signals, while the other belongs to the on-chip optical network bus waveguide, which is used to transmit the modulated optical signals. There is a suitable distance between the two waveguides for the gap to achieve optical signal coupling by the coupling mode principle. The thickness and width of the waveguide are set to H_g and W_g respectively, and the metal-oxide-semiconductor ITO activation area is designed on top of the waveguide in the modulation area. From the top to the bottom, they are Au, HfO_2, ITO, HfO_2, Au, and HfO_2, and the thicknesses of Au, HfO_2, ITO are H_{Au}, H_{HfO_2}, and H_{ITO} respectively. The bottom Au thickness is 5 nm. Different from

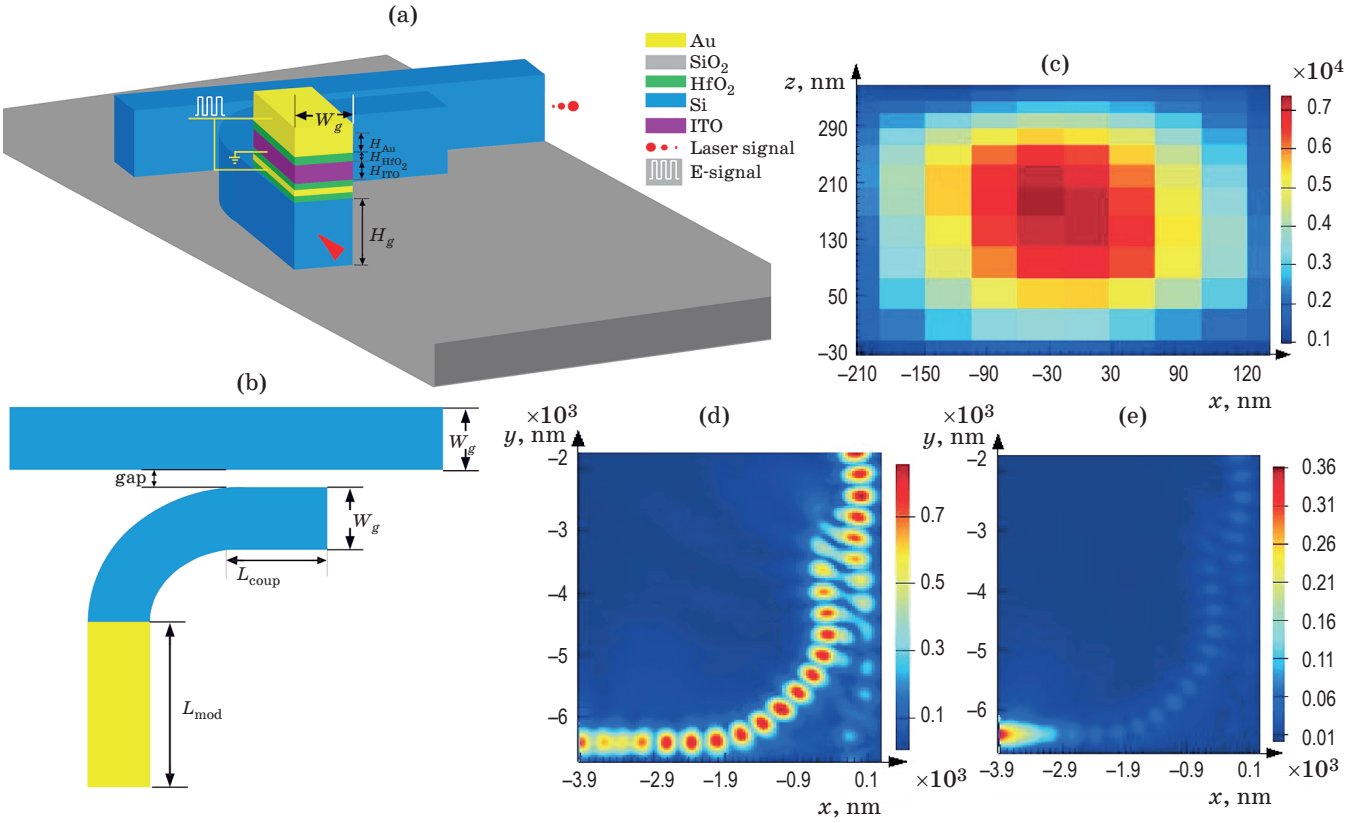

Fig. 2. Structure of directional coupled SPP electro-optic modulator. (a) 3D model of the EOM structure, (b) 2D model of the EOM structure, (c) Z-direction cross-sectional view of an optical signal passing through a silicon-based waveguide, (d) light field distribution of the EOM in the ON state, (e) light field distribution of the electro-optic modulator in the OFF state.

the previous EOMs proposed by scholars, in this design, an additional Au electrode was added to the middle of the bottom layer of HfO_2 to reduce the electrode resistance and increase the modulation rate. As shown in Fig. 2a, the carrier concentration of the ITO-activated material is regulated by the voltage. The ON and OFF states are simulated by simulation software. The optical field distribution diagrams are shown in Figs. 2d, e. Figure 2d shows two states that are ON when a voltage is applied, and Fig. 2e is the OFF state when no voltage is applied. Figure 2c shows the distribution of the optical signal in the silicon waveguide. It can be seen from the figure that the optical signal energy is almost completely bound in the waveguide.

Device theory analysis

From the analysis of the designed device model structure, the working principle of the EOM is mainly designed according to coupled mode theory and the electrical regulation principle of TCOs.

Coupled mode theory

According to perturbation theory, the coupling system can be used as an ideal waveguide for some kinds of perturbation. The wave equation for a dielectric optical waveguide can be used [15]

$$\nabla^2\mathbf{E}(\mathbf{r},t)=\mu_0\varepsilon_0\frac{\partial^2\mathbf{E}(\mathbf{r},t)}{\partial t^2}+\mu_0\frac{\partial^2}{\partial t^2}\mathbf{P}(\mathbf{r},t), \quad (1)$$

where the $\mathbf{E}$ is intensity of the electric field, μ_0 is permeability of free space, ε_0 is permittivity of free space, $\mathbf{r}$ is vector radius, and t is the time variable.

Under the effect of perturbation, the polarization intensity $\mathbf{P}(\mathbf{r}, t)$ of the medium in the waveguide undergoes a perturbation variation, which can be expressed as

$$\mathbf{P}(\mathbf{r},t)=\mathbf{P}_0(\mathbf{r},t)+\mathbf{P}_{\text{pert}}(\mathbf{r},t), \quad (2)$$

where $\mathbf{P}_0(\mathbf{r}, t)$ represents the polarization intensity of the medium in the waveguide when

there is no disturbance and $\mathbf{P}_{\text{pert}}(\mathbf{r}, t)$ represents the additional polarization intensity caused by various disturbances related to the coupled wave. According to Eqs. (1) and (2), E_x, E_y, and E_z can be derived as follows:

$$\nabla^2 E_x - \mu_0 \varepsilon(r) \frac{\partial^2 E_x}{\partial t^2} = \mu_0 \frac{\partial^2}{\partial t^2} \left[\mathbf{P}_{\text{pert}}(\mathbf{r}, t)\right]_x, \quad (3)$$

$$\nabla^2 E_y - \mu_0 \varepsilon(r) \frac{\partial^2 E_y}{\partial t^2} = \mu_0 \frac{\partial^2}{\partial t^2} \left[\mathbf{P}_{\text{pert}}(\mathbf{r}, t)\right]_y, \quad (4)$$

$$\nabla^2 E_z - \mu_0 \varepsilon(r) \frac{\partial^2 E_z}{\partial t^2} = \mu_0 \frac{\partial^2}{\partial t^2} \left[\mathbf{P}_{\text{pert}}(\mathbf{r}, t)\right]_z, \quad (5)$$

The optical field in a perturbed waveguide is expanded into a linear superposition of all possible modes of electromagnetic fields in the waveguide, and then equation (4) and the orthogonality between the wave fields of each mode are used to produce a "gradual change" in the wave field amplitude caused by the mode coupling. Under the condition

$$\left|\frac{d^2 \mathbf{A}_m}{dz^2}\right| \ll \beta_m \left|\frac{d\mathbf{A}_m}{dz}\right|, \quad (6)$$

where $\mathbf{A}_m$ is the mode amplitudes of m-order modes, z is the free space z direction, and β_m is m-order modes propagation constant.

After analysis and derivation, we can obtain [16, 17]

$$\begin{aligned} &\frac{dA_m^{(-)}}{dz} \exp\left[j(\omega t + \beta_m z)\right] - \\ &- \frac{dA_m^{(+)}}{dz} \exp\left[j(\omega t + \beta_m z)\right] - c.c = \\ &= -\frac{j}{2\omega} \frac{\partial^2}{\partial t^2} \int_{-\infty}^{\infty} \left[\mathbf{P}_{\text{pert}}(\mathbf{r}, t)\right]_y E_y^s(x) dx, \end{aligned} \quad (7)$$

where ω is angular frequency, $c.c$ is the conjugate complex term of the former term. The left two terms in the above formula represent a wave $(A_m^{(-)})$ propagating in the $-z$ direction and a wave $(A_m^{(+)})$ propagating in the $+z$ direction. $(A_m^{(-)})$ and $(A_m^{(+)})$ are the amplitude functions of the m-order mode wave in two directions respectively.

The designed electro-optic modulation structure can be regarded as two waveguides a and b that are close to each other, as shown in Fig. 3a, and the refractive indices of the two waveguides are n_a and n_b respectively. When the distance between the two waveguides is long enough, no coupling occurs. The intensity of the wave fields are $E_y^{(a)}(x)$ and $E_y^{(b)}(x)$, and two waveguide modes will propagate independently with their propagation constants β_a and β_b. When the two waveguides are close enough, a coupling phenomenon occurs, and the optical field can be approximately expressed as the sum of the two light fields without disturbance, that is,

$$\begin{aligned} \mathbf{E}_y = &\mathbf{A}(z) E_y^{(a)}(x) \exp\left[-j\beta_a z\right] + \\ &+ \mathbf{B}(z) E_y^{(b)}(x) \exp\left[-j\beta_b z\right], \end{aligned} \quad (8)$$

$\mathbf{A}(z)$ and $\mathbf{B}(z)$ are the mode amplitudes of the two waveguides respectively. According to Eqs. (1) and (2), the perturbation polarization intensity $\mathbf{P}_{\text{pert}}(\mathbf{r}, t)$ can be obtained as

$$\begin{aligned} \mathbf{P}_{\text{pert}} = \varepsilon_0 \Big[&E_y^{(a)} \mathbf{A}(z)(n^2(x) - n_a^2(x)) \exp(-j\beta_a z) + \\ &+ E_y^{(b)} \mathbf{A}(z)(n^2(x) - n_b^2(x)) \exp(-j\beta_b z) \Big], \end{aligned} \quad (9)$$

where $n(x)$ is the refractive index distribution function of the coupled waveguide. By substituting this into Eq. (7), we obtain the coupling equations as

$$\frac{d\mathbf{A}}{dz} = -jK_{ab}\mathbf{B} \exp\left[-j(\beta_b - \beta_a)z\right] - jM_a\mathbf{A}, \quad (10)$$

$$\frac{d\mathbf{B}}{dz} = -jK_{ba}\mathbf{A} \exp\left[-j(\beta_a - \beta_b)z\right] - jM_b\mathbf{B}, \quad (11)$$

where, the coupling coefficient in the formulas is

$$K_{ba.ab} = \frac{\omega\varepsilon_0}{4} \int_{-\infty}^{\infty} \left[n^2(x) - n_{a,b}^2(x)\right] E_y^{(a)} E_y^{(b)} dx, \quad (12)$$

where M_a and M_b in Eqs. (10) and (11) represents are self-coupling coefficients, and the wave transmission coefficients relative to the uncoupled waveguides β_a and β_b will change to $\beta_a + M_a$ and $\beta_b + M_b$ respectively, therefore

$$M_{ab} = \frac{\omega\varepsilon_0}{4} \int_{-\infty}^{\infty} \left[n^2(x) - n_{a,b}^2(x)\right] \left[E_y^{(a,b)}\right]^2 dx, \quad (13)$$

where $E_y^{(a,b)}(x)$ is the intensity of the coupling wave fields. the difference between the trans-

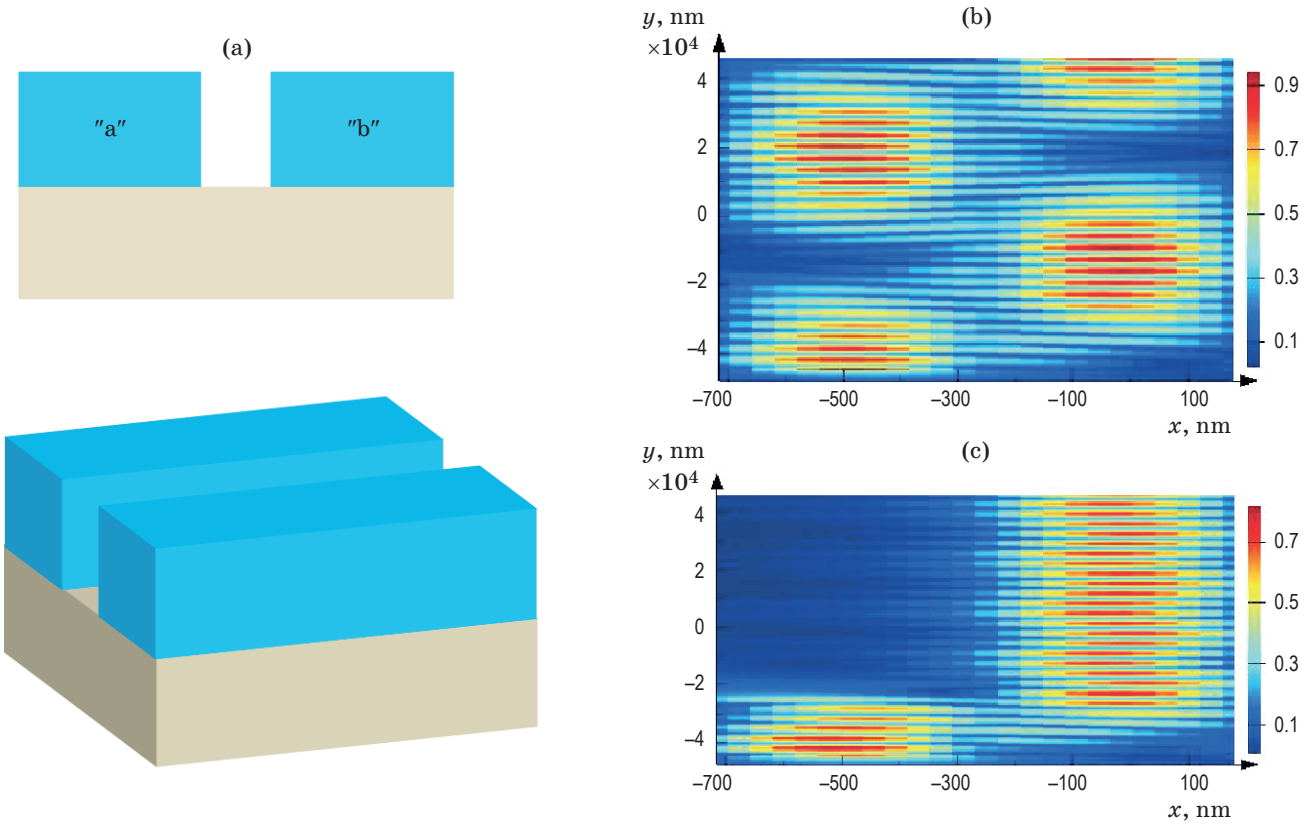

Fig. 3. Optical coupling model and electromagnetic field distribution of silicon based double waveguides. (a) Silicon-based dual-waveguide optical coupling model, which includes a substrate and two silicon waveguides "a" and "b", (b) dual-waveguide coupling light field distribution, (c) single-cycle coupling, where the optical signal continues to propagate along the other waveguide.

mission constants of the waveguide modes of the a and b waveguides is

$$2\delta = (\beta_b + M_b) - (\beta_a + M_a). \tag{14}$$

The wave energy transfer caused by mode coupling can occur only when a close match occurs, that is, when phase-mismatch factor $\delta = 0$.

Assume that only waveguide a has single-mode optical propagation at $z = 0$ and that the perturbation occurs in the area where $z > 0$, that is

$$\mathbf{B}(0) = \mathbf{B}_0, \quad \mathbf{A}(0) = \mathbf{A}_0. \tag{15}$$

The energies of the optical waves in waveguides a and b are respectively represented by $P_a = |\mathbf{A}(z)|^2$ and $P_b = |\mathbf{B}(z)|^2$. According to the principle of energy conservation, the following can be obtained

$$\frac{d}{dz}\left(|\mathbf{A}(z)|^2 + |\mathbf{B}(z)|^2\right) = 0. \tag{16}$$

When the waveguides a and b have the same size and refractive index structure and their material parameters are the same, the coupling coefficient is

$$K_{ba} = K_{ab}, \quad M_{ab} = M_{ba}. \tag{17}$$

According to the above conditions, the solution to the coupling equation (10) is

$$\mathbf{A}(z) = \mathbf{B}_0 \frac{K}{(K^2 + \delta^2)^{\frac{1}{2}}} \times \times \exp(-j\delta z) \sin\left[(K^2 + \delta^2)^{\frac{1}{2}} z\right], \tag{18}$$

$$\mathbf{B}(z) = \mathbf{B}_0 \exp(j\delta z)\{\cos\left[(K^2 + \delta^2)^{\frac{1}{2}} z\right] - -j\frac{\delta}{(K^2 + \delta^2)^{\frac{1}{2}}} \sin\left[(K^2 + \delta^2)^{\frac{1}{2}} z\right], \tag{19}$$

where $K^2 = |K_{ab}|^2$. The energy carried in waveguides a and b is expressed as

$$P_a(z) = P_0 \frac{K^2}{K^2 + \delta^2} \sin^2\left[(K^2 + \delta^2)^{\frac{1}{2}} z\right], \quad (20)$$

$$P_b(z) = P_0 - P_a(z). \quad (21)$$

In the above formulas, $P_0 = |\mathbf{A}(0)|^2$ is the input energy of waveguide "a". In phase matching, that is, when the propagation constants of the two waveguides are equal, the transmission distance is $\pi/2K$ [13]. As shown in Figs. 3b, c, the energy is completely transferred from waveguide "a" to waveguide "b".

To ensure that the modulator does not affect the optical signal of other modulators in the ring waveguide, according to the coupling distance formula $\pi/2K$, the coupling distance can be set to $L_{\text{coup}} = n\pi/2K$. To reduce the loss caused by multiperiod coupling, we set n to 1. The simulation results show that the scheme is feasible and that almost no optical signal is detected in the modulation area; hence, the local modulator will not affect the optical signal transmission of other modulators in the ring waveguide. This parameter is discussed in detail in section "Device parameter optimization".

Transparent conducting oxide electrical regulation principle

The active material ITO is a transparent conducting oxide (TCO) with a dielectric constant electrical tuning characteristic. As shown in Fig. 4a, the structure is a scheme adopted in the design, and it has a similar field effect to that of silicon-based metal-oxide-semiconductors (MOSs). When an applied voltage is applied, the carrier accumulation area or depletion area can be formed rapidly at the interface between the TCO material layer and the dielectric layer. The carrier concentration in the accumulation area or depletion area can be regulated by the applied bias voltage, and then the dielectric constant (refractive index) of TCOs can be changed. When the real part of the dielectric constant of the TCO material layer is close to zero, it is defined as the near-zero dielectric constant state (epsilon-near-zero). The near-zero state of the dielectric constant can greatly enhance the overlapping integration of the optical field and the electro-optical material layer, effectively improving the optical absorption and modulation efficiency. Therefore, most EOMs based on TCO materials usually use SiO_2 slit waveguides [14, 17–20] or hybrid photonic-plasmonic structures to construct MOS capacitor structures and apply appropriate voltages to obtain the near-zero dielectric constant of the TCO material to achieve electrical absorption modulation. Its dielectric constant conforms to the Drude model [17]

$$\varepsilon = \varepsilon_\infty - \frac{N_{\text{ITO}} q^2}{(\omega^2 + i\omega\gamma)\varepsilon_0 m^*}. \quad (22)$$

In the above formula, ε_∞ is the high-frequency dielectric constant ($\varepsilon_\infty = 3.9$), N_{ITO} is the electron concentration of the ITO material, ω is the angular frequency, γ is the carrier scattering rate ($\gamma = 1.8\times10^{14}$ rad/s), m^* is the effective carrier mass ($m^* = 0.35m_0$, where m_0 is the electron mass, $m_0 = 9.31\times10^{-31}$ kg), q is the electronic charge ($q = 1.6\times10^{-19}$ C), and ε_0 is the free-space dielectric constant ($\varepsilon_0 = 8.85\times10^{-12}$ F/m).

To calculate the variation in ITO carrier concentration controlled by the voltage, according to Ref. [14], we use the following simple model:

$$N_{\text{ITO}} = N_0 + \frac{\varepsilon_0 K_{\text{HfO}_2} V_g}{q H_{\text{HfO}_2} H_{\text{acc}}}. \quad (23)$$

According to Ref. [14], $N_0 = 1.6\times10^{19}\text{cm}^{-3}$ is the carrier concentration of ITO. H_{HfO_2} is the thickness of the insulation layer HfO_2 in the model structure, and H_{acc} is the thickness of the free carrier accumulated by HfO_2 under the ITO surface. According to Refs. [21, 22], $H_{\text{acc}} = 7$ nm; this thickness can also be obtained from the following simulation studies. In addition, according to Ref. [21], HfO_2 has a high relative dielectric constant ($K_{\text{HfO}_2} = 25$). Therefore, Lumerical's device software was used to simulate the change in ITO carrier concentration of the applied voltage. The doping concentrations of Au, ITO, and HfO_2 are shown in Fig. 4a, the voltage is increased from 0 to 5 V, and the carrier concentration is plotted in Fig. 4c. During the experiment, we doped the initial concentration of ITO to 1.6×10^{19} cm^{-3} and defined this state of ITO concentration as 0 V. According to formula (21), the effec-

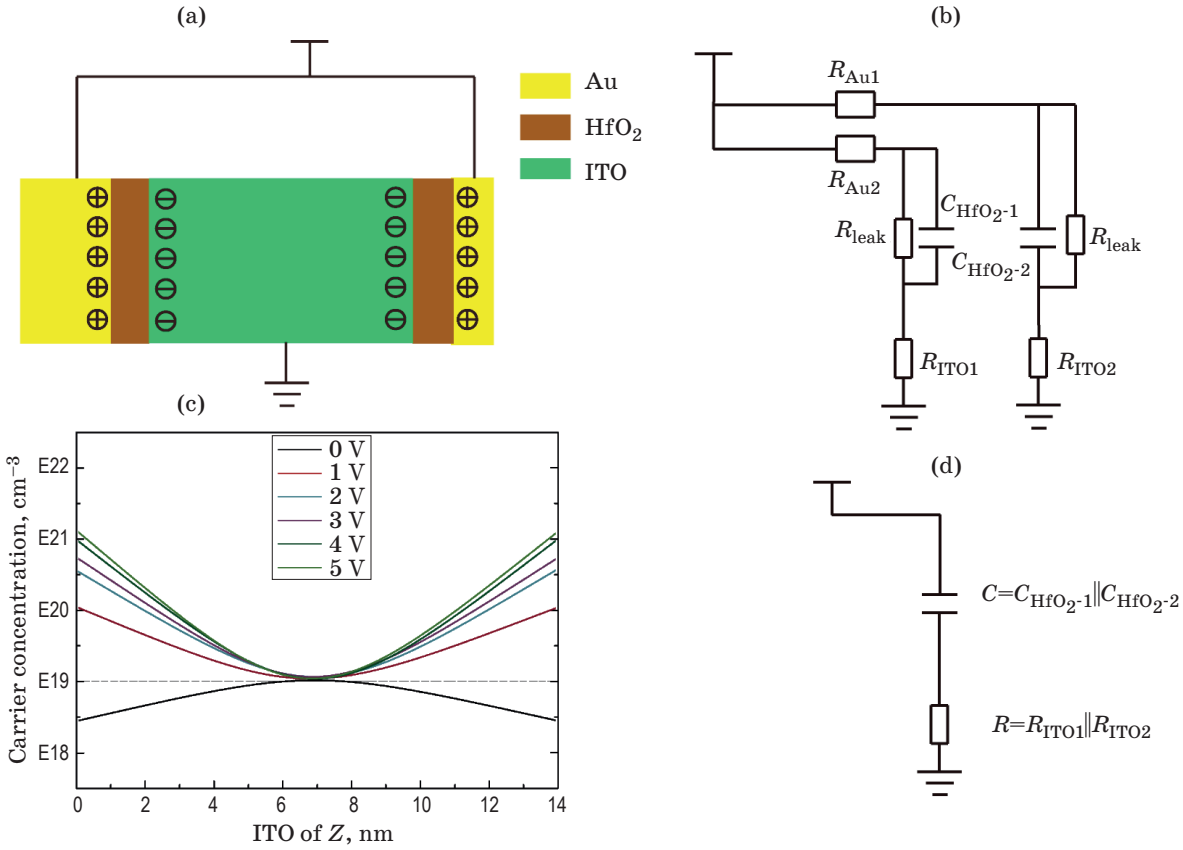

Fig. 4. ITO film voltage application equivalent circuit. (a) Voltage application method of the active material ITO, (b) equivalent circuit of the MOS capacitor structure, (c) carrier concentration change under different voltage conditions, (d) simplification of the equivalent circuit.

tive refractive index corresponding to ITO is $1.90509 + 0.0036i$ at this ITO concentration, which is the modulator ON state. When the voltage is increased to 2.35 V, the carrier concentration is 5.57×10^{22} cm^{-3}, the real part of the dielectric constant of the ITO material layer is close to zero (epsilon-near-zero), and the corresponding effective refractive index is $0.478 + 0.6184i$, which is the OFF state of the modulator. In the following simulation experiments, the refractive index of the ITO-activated thin-film material is set based on the two parameters described above.

DEVICE PARAMETER OPTIMIZATION AND DISCUSSION

To study the influence of various parameters of the model structure on the device performance, we use Lumerical's 3D-FDTD simulation software [23] based on Maxwell's equations to conduct a detailed simulation. In the simulation process, to obtain more accurate simulation results, we set the mesh order of the simulation software to 3 and the boundary condition to 12. The effects of the coupling distance L_{coup} in the structure of the research model and the effect of the gap parameter gap on the coupling strength of the two waveguides are studied separately, and then the effect of L_{mod} on the extinction ratio is studied. Finally, the effects of the thickness parameters of H_{ITO} and H_{HfO_2} on the extinction ratio and transmittance are studied. Through the above research and analysis, we discuss the device parameters based on the optimized model structure parameters.

Device parameter optimization

As a first optimization step, we study the coupling distance L_{coup} in the model structure. During the experiment, we set L_{coup} as follows: $L_{coup} = 3000$, $L_{coup} = 3200$, $L_{coup} = 3500$, $L_{coup} = 3600$, and $L_{coup} = 3800$ nm. Then, for each experiment, the TM mode light source was placed at the three port entrances, and trans-

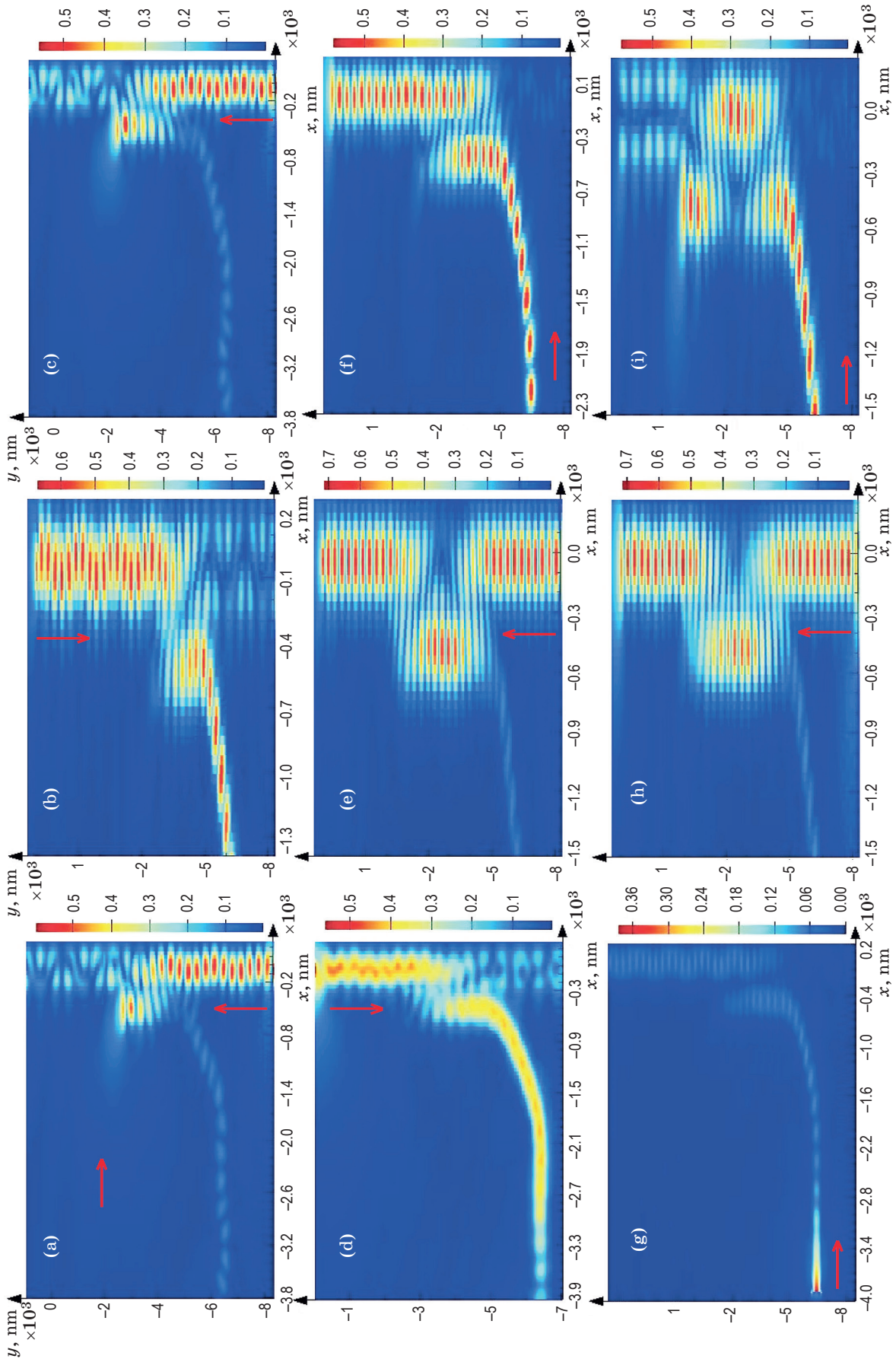

Fig. 5. Light field distribution under different L_{coup} values. (a) and (b) $L_{coup} = 3000$ nm, (c) and (d) $L_{coup} = 3200$ nm, (e), (f), (g), and (h) $L_{coup} = 3500$, 3550, 3550, and 3600 nm respectively. When the optical signal is transmitted to the coupling area, the optical signal transmission path is still destroyed, but the optical signal is almost completely coupled back to the curved waveguide. The optical signal can continue to transmit in the straight waveguide, which is the original intention of the design. (i) $L_{coup} = 3800$ nm. The optical signal is injected from the curved waveguide, the optical signal in the straight waveguide is affected by the modulator, and the optical signal cannot continue to propagate.

mission of the optical signal through the detector was observed. After the simulation, the experimental results were obtained, as shown in Fig. 5 (a–i). As shown in Figs. 5a, b, when $L_{coup} = 3000$ nm, the optical signals are transmitted from the bottom to the top and vice versa in a straight waveguide. When the optical signal is transmitted to the coupling area, the optical signal transmission path is destroyed, and the optical signal cannot continue to transmit well. This situation is not the original intention of the design.

As shown in Figs. 5c, d, the coupling distance L_{coup} is increased such that $L_{coup} = 3200$ nm. When the optical signal is transmitted to the coupling area, the transmission path of the optical signal is still destroyed, but the energy of the optical signal continues to transmit in the straight waveguide and is strengthened. From Fig. 5e, the coupling distance is again increased such that $L_{coup} = 3500$ nm. When the optical signal is transmitted to the coupling area, the optical signal transmission path is still destroyed, but the optical signal is almost completely coupled back to the curved waveguide. The optical signal can continue to transmit in the straight waveguide, which is the original intention of the design. To verify the coupling of the modulator, the light source is input from the modulation area and set to the ON and OFF states, as shown in Figs. 5f, g. When the optical signal is in the ON state, the optical signal can almost be completely coupled to the straight waveguide, as shown in Fig. 5f. Since the optical signal is in the OFF state, almost no optical signal is observed in the coupling region, the curved waveguide and the straight waveguide, as shown in Fig. 5g. The coupling distance is further increased to 3600 nm, and the optical signal in the straight waveguide is not affected by the modulator. When the coupling distance is increased to 3800 nm, the optical signal is injected from the straight waveguide, and we find that the optical signal in the straight waveguide is affected by the modulator and that the optical signal cannot continue to propagate. Through the above simulation research, combined with formula [16], when the coupling distance $L_{coup} = \pi/2K$, the optical energy is completely coupled from one waveguide to the other waveguide, and $L_{coup} = n\pi/2K + X$ causes a part of the optical signals to not be completely coupled, which causes the optical signals in the ring waveguide to be transmitted to the modulation area and affects the optical signal transmission in the ring waveguide. At the same time, the above simulation results provide a reference for the position of the modulator coupling region in an ORNoC.

Through the above experimental research, it can be determined that when the coupling distance L_{coup} is set between 3500 and 3600 nm, the device can both achieve coupling between the modulation area and the ring waveguide and achieve the optical signal transmission of other modulators in the ring waveguide.

For the coupling strength, the key influencing factor is the gap between the waveguide in the modulation area and the ring waveguide; thus, we can observe the modulator's transmission by changing the gap size. In the simulation experiment, the gap was set from 68 to 28 nm, with increments of 5 nm; the simulation results and the processed results are plotted in Figs. 6 and 7 respectively. From Figs. 6 and 7, when the gap is successively reduced from 68 to 38 nm, the transmittance is gradually enhanced. When the gap is changed from 38 to 28 nm in turn, the transmittance decreases. According to the coupling mode theory [16] and Eqs. (8) and (9), with the decrease in the gap, the coupling strength is increased exponentially. In fact, when the optical modes of the two waveguides remain unchanged, the gap is continuously reduced, which causes the two optical films to compress each

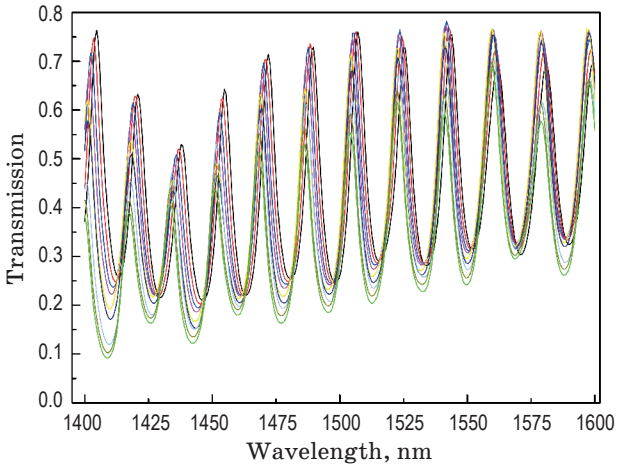

Fig. 6 Transmission at various wavelengths under different coupling distance gaps (black — 28 nm, red — 33 nm, cyan — 38 nm, pink — 43 nm, yellow — 48 nm, blue — 53 nm, pale cyan — 58 nm, olive — 63 nm, green – 68 nm).

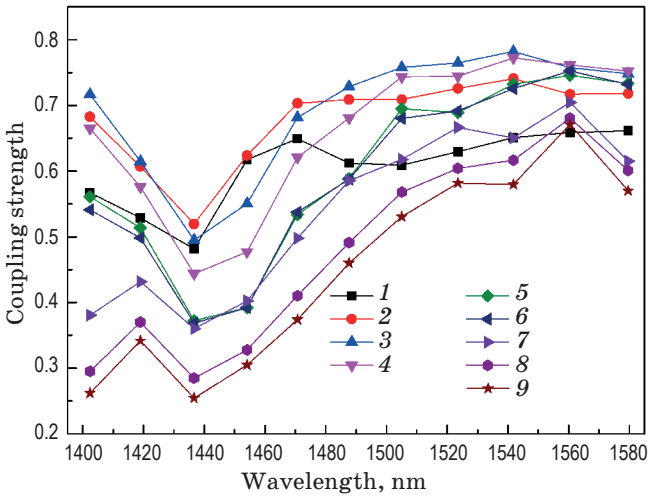

Fig. 7. Normalized transmission curves with different coupling distance gaps. (*1* — 28 nm, *2* — 33 nm, *3* — 38 nm, *4* — 43 nm, *5* — 48 nm, *6* — 53 nm, *7* — 58 nm, *8* — 63 nm, *9* — 68 nm).

other, leading to the failure of the coupled mode theory [16].

The gap between the waveguide in the modulation region and the ring waveguide should be set to 38 nm on the basis of the above experimental research. If the gap between the waveguide and the ring waveguide in the modulation area is set between 33 and 43 nm, the optical wavelength coupling strength between 1500 and 1600 nm is approximately 0.65 to 0.7, and the phase difference is only 0.5, which is very advantageous for the fabrication of the actual electro-optical modulator.

To reduce the simulation time and obtain more accurate experimental results, only the modulation area is simulated when the thickness of the ITO-activated material is studied. This method is equivalent to the simulation of the entire device, and the thickness of the ITO-activated material mainly affects the ER/IL and switching rate of the modulator. According to the literature [17, 19, 20], the thickness of the ITO-activated material of most SPP EOMs is generally set between 10 and 25 nm; thus, during the experiment, the thickness of the ITO-activated material was set to 10, 15, 20, and 25 nm. After changing the thickness of each ITO-activated material and using the detector to collect the transmittances in the ON and OFF states, the results are as plotted in Fig. 8. Then, formulas (24) and (25) are used to calculate the ER and IL, and the results are plotted in Fig. 9. From Fig. 8, when the thickness of the ITO-activated material gradually increased from 10 nm, the transmittance of the optical signals in the ON state and the OFF state gradually increased. The reason is that as the thickness of the ITO-activated material film increases, the SPP effect at the top Au–ITO interface weakens, which leads to the weakening of the ability of ITO-activated material to control the optical sig-

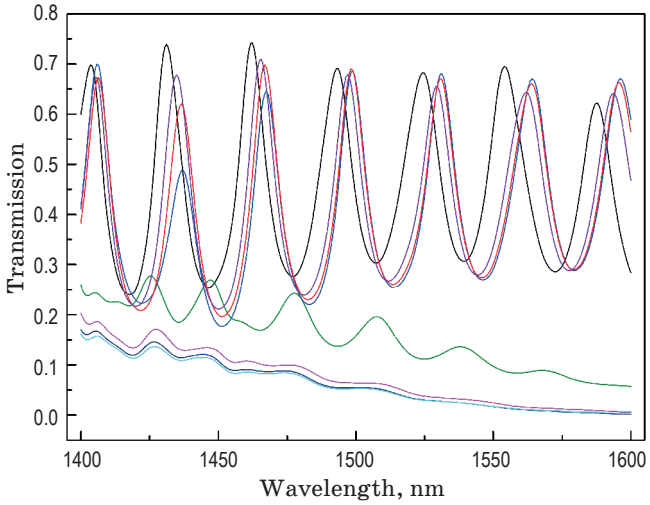

Fig. 8. Transmission curves of the ON (black — 25 nm, cyan — 20 nm, red — 15 nm, purple — 10 nm) and OFF (green — 25 nm, pink — 20 nm, blue — 15 nm, bright cyan — 10 nm) states for different ITO thicknesses.

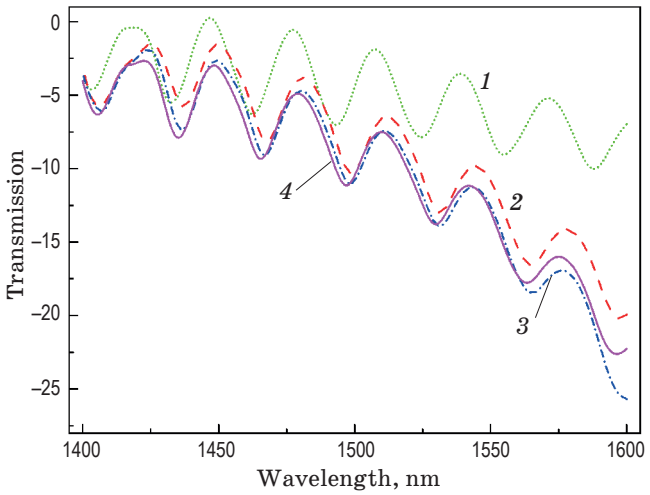

Fig. 9. Extinction coefficients for different ITO thicknesses. *1* — 25 nm, *2* — 20 nm, *3* — 15 nm, *4* — 10 nm.

nal in the waveguide and results in the increase in the transmittance of the optical signal in the ON state and the OFF state at the same time. However, from the curve observed in Fig. 9, it is found that the ER decreases as the thickness of the ITO-activated material film increases and that the average ER between 10 and 15 nm is 0.2 dB. The thickness of the activated material film is preferably 15 nm.

When studying the effect of the HfO_2 thickness on device performance, to reduce the simulation experiment time and obtain accurate experimental results, only the modulation area is simulated. This method is equivalent to the simulation of the entire device. The HfO_2 thickness mainly affects the modulator's ER/IL and switching rate. According to Refs. [14, 16, 17], the insulation layer of most SPP EOMs is set between 10 and 20 nm; thus, during the experiment, the thickness of HfO_2 is set between 10 and 20 nm, with increments of 1 nm. After changing the thickness of each HfO_2 layer, the detector is used to collect the transmittances in the ON and OFF states, and the results are plotted in Fig. 9. Then, we use the formulas to calculate the ER and IL, the results of which are plotted in Fig. 10. From the results in Fig. 10, when the thickness of HfO_2 increases sequentially from 10 nm, the transmittance of optical signals in the ON state and OFF state increases exponentially. The reason is that as the thickness of the HfO_2 layer increases, the ITO-activated material film gradually moves away from the silicon waveguide; thus, the ability of the ITO-activated material film to control the optical signal decreases exponentially with the distance.

The variation in the ER and IL in Fig. 11 shows that as the thickness of HfO_2 increases, the IL gradually decreases. The ER is the largest between 12 and 15 nm, *i.e.*, approximately –11.5 dB, and the IL is approximately –2.2 dB. From the figure, the optimal value of the HfO_2 thickness should be 14 nm.

To study the effect of the length of the modulation area L_{mod} on the performance of the modulator, in the simulation experiment, the length of

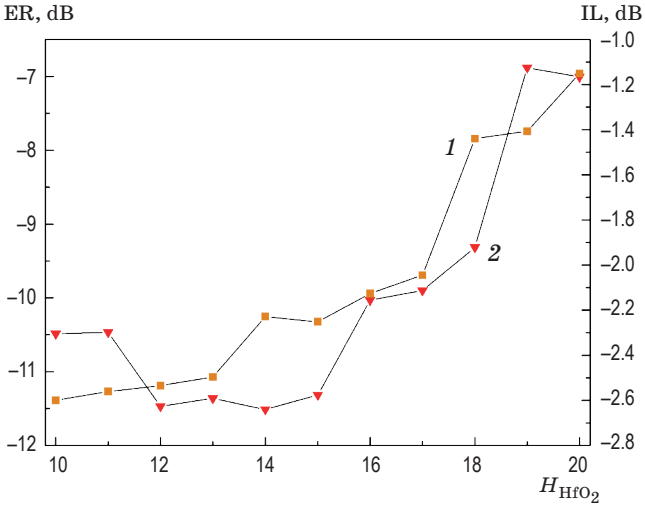

Fig. 11. The insertion loss (*1*) and the extinction ratio (*2*) for different HfO_2 insulation layer thicknesses.

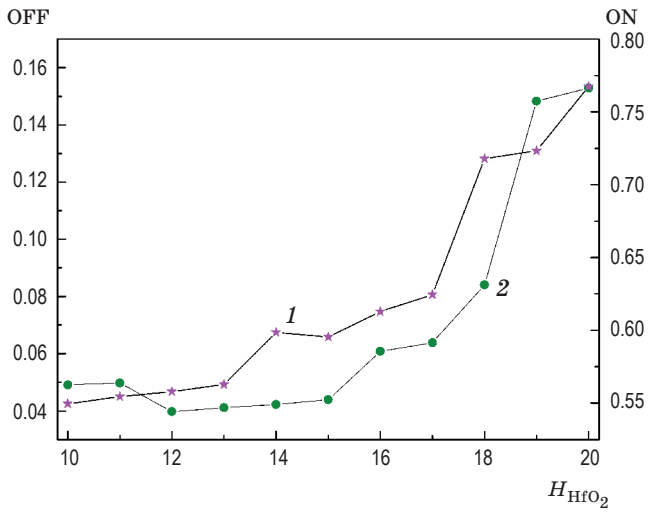

Fig. 10. Transmission curves for different HfO_2 insulation layer thicknesses. ON – *1*, OFF – *2*.

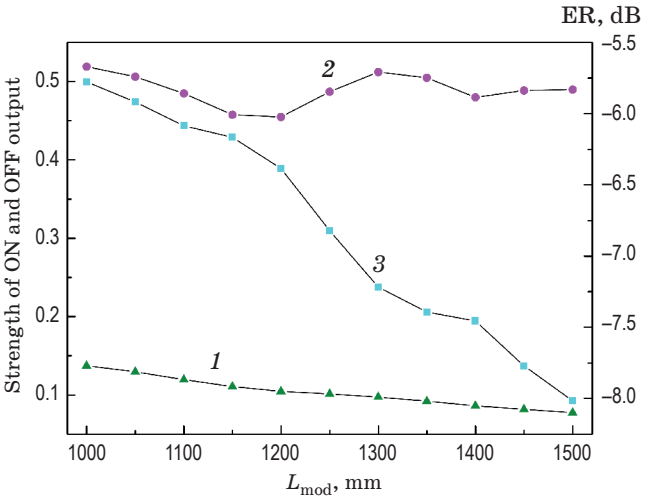

Fig. 12. Output strength in the OFF (*1*) and ON (*2*) states and ER (*3*) of L_{mod} for different lengths.

L_{mod} is set between 1000 and 1500 nm, starting from 1000 nm and increasing by 50 nm in each iteration. The output intensity of the modulator is recorded in each experiment. After the values are normalized, the output strength in the OFF (*1*) and ON (*2*) states and the ER (*3*) are plotted in Fig. 12. The change in the curve in the figure shows that the output intensity of the OFF state decreases as the length of the modulation length increases. In the ON state, the output intensity is extremely high when $L_{mod} = 1300$ nm. To miniaturize the device and lower the insertion loss, it should be set between 1300 and 1400 nm. In this design, the modulation length L_{mod} of this device should be set to 1350 nm.

Device performance analysis

The extinction ratio, insertion loss, and modulation rate are the key parameters for measuring the performance of EOMs. According to the definition of the ER, the ER can be expressed by the following formula [24]:

$$\mathrm{ER} = 10\log\frac{P_{off}}{P_{on}}. \quad (24)$$

Additionally, according to the definition of the insertion loss, the IL can be expressed by the following formula:

$$\mathrm{IL} = 10\log\frac{P_{on}}{P_{inj}}. \quad (25)$$

In the above formula, P_{off} is the intensity of the optical signal in the ring waveguide when it is in the OFF state, P_{on} is the intensity of the optical signal in the ring waveguide when it is in the ON state, and P_{inj} is the intensity of the optical signal injected into the modulation end.

According to the literature [24–26], the switching rate of the EOM designed in this paper can be calculated as the switching rate of the MOS structure junction, which is expressed by the following formula:

$$f_{max} = \frac{1}{2\pi RV}. \quad (26)$$

From the formula defining the capacitor, we obtain

$$V = \frac{\varepsilon_0 \varepsilon A}{H_{HfO_2}}. \quad (27)$$

In the formula (27), $\varepsilon_0 = 8.85\times10^{-12}$ F/m, H_{HfO_2} is the thickness of HfO_2, A is the capacitance junction area, $A = W_{gi}L_{mod}$.

According to Ref. [27] and the equivalent circuit in Fig. 4d, we know that the electrode resistance R is the equivalent resistance of the ITO-activated material film and can be expressed as

$$R = \frac{L}{\sigma A}. \quad (28)$$

In the above formula, L is half the thickness of the ITO-activated material film, that is, $L = H_{HfO_2}/2$, A is the cross-section area of the ITO-activated material film perpendicular to the Z direction of the device, σ is the conductivity of the ITO-activated material film, that is, $\sigma = ñq\mu_n$, and $ñ$ is the carrier concentration, which can be assumed as $N_0 = 1.6\times10^{19}\mathrm{cm}^{-3}$. In fact, when a certain voltage is applied to the nonintrinsic semiconductor, the carrier concentration will be much greater than the initial concentration [21]. Therefore, the equivalent resistance of the activated material thin film is smaller than that calculated theoretically. According to Ref. [27], the carrier mobility of ITO-activated material films is $\mu_n = 20$ cm^2 per volt and per second. According to the above formula, we can determine that the contact resistance of ITO is approximately 200 Ω.

According to Ref. [12], the power consumption required to transmit 1 bit can be calculated according to the amount of energy charged by the capacitor (no energy is required to discharge), which can be expressed as

$$E = \frac{1}{2}VU^2. \quad (29)$$

From formula (27), the capacitance value $V = (\varepsilon_0\varepsilon A)/H_{HfO_2} = 2.0719\times10^{-15}$, $U = 3.5$ V, and $E = 12.69\times10^{-15}$ J, that is, 1 bit transmission is required, and the power consumption is 12.69 fJ.

The parameters listed in Table 1 are optimized model structure parameters. Using the parameters in the table, the EOM is simulated again. The coupling spectrum and transmission spectrum curves of the ON and OFF states are plotted in Fig. 13 and calculated according to

formulas (24) and (25), The ER and IL curves of the EOM are plotted in Fig. 14.

It can be seen from the optical signal coupling curve of Fig. 13 that at a wavelength of 1550 nm, the coupling efficiency of the EOM exceeds 90%. When the EOM is in the ON state, the transmittance is greater than 75% at a wavelength of 1550 nm, while in the OFF state, the transmittance is less than 1% at a wavelength of 1550 nm. As can be seen from Fig. 14 and the ER and IL curves, the ER becomes larger as the wavelength changes, and ER = −15.4 dB at a wavelength of 1550 nm. From the IL curve in Fig. 14, it can be seen that IL = −1.17 dB at a wavelength of 1550 nm, which remains broadly unchanged. Based on the above theoretical analysis and optimization of the structural parameters of the model, the performance parameters of the designed EOM obtained by simulation are as listed in Table 2 and compared with the parameters of EOMs designed in other studies.

We can see from Table 2 that the parameters of the EOM designed in this paper are significantly better than those of other EOMs designed by

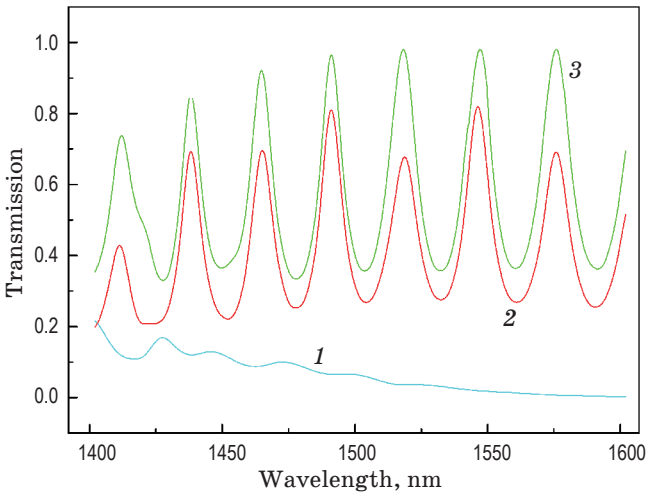

Fig. 13. Transmission curves of the states OFF (*1*), ON (*2*), and IN (*3*) of the device after the structural parameters of the model are optimized.

Table 1. List of the design parameters for the designed electro-optic modulator

Parameter	Value
Width of waveguide, nm	400
Width of gap, nm	38
Height of waveguide, nm	180
Height of HfO_2, nm	14
Height of Au, nm	100
Height of ITO, nm	15
L_{coup}, nm	3550
L_{mod}, nm	1350

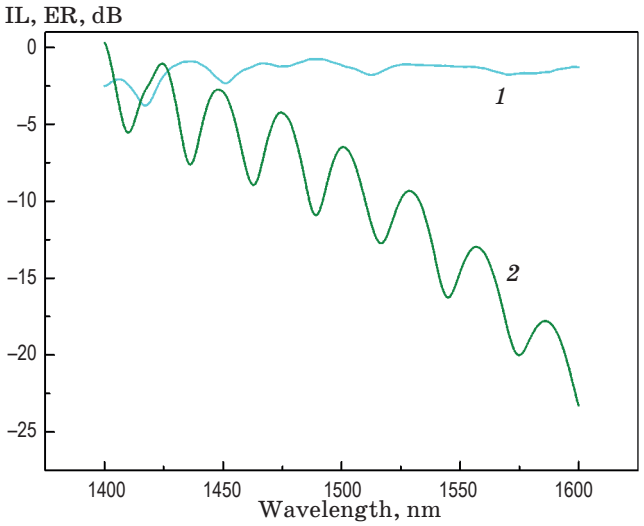

Fig. 14. The insertion loss (*1*) and the extinction ratio (*2*) of the device after the structural parameters of the model are optimized.

Table 2. Summary of the proposed modulator parameters compared with those of other ITO-based modulators

ER, dB	IL, dB	*E*, fJ	f_{max}, Tbit/s	*L*, μm	V_g, V	λ, nm	References
6.7	0.032	78.9	0.116	17.6	2.4	1310	[17]
6.14	0.06	67.1	0.0475	21	2.35	1550	[19]
5	0.87	330	0.257	5.6	2.3	1550	[20]
9.14	0.86	4.35	1	5	2.35	1550	[12]
15.4	1.17	**12.69**	**0.75**	**3.89**	2.35	1550	This work

other scholars. In addition, the insertion loss is 0.3 dB higher than that in Ref. [20], which is mainly caused by the coupling loss between the two waveguides.

CONCLUSIONS

To realize the application of SPP EOMs on an ORNoC, a directional coupling EOM is designed, which achieves high-speed switching from both the ON and OFF states. While the local EOM effectively couples the optical signal to the ring waveguide, the optical signal of the other EOM is not affected and thus can continue transmission in the waveguide. The 3D-FDTD simulation software proves the feasibility of the scheme. By improving the applied voltage, the electrode contact resistance is effectively reduced, and the modulator speed of the device is significantly increased. The optimal performance and size parameters are obtained by optimizing the design of the device and finally solved by the simulation software. The experimental results show that the coupling efficiency is greater than 90%, the IL is 1.17 dB and the ER is 15.4 dB at a wavelength of 1550 nm. The modulation rate is as high as 0.75 Tbit/s, and the size is only 3.8×3.2×1.2 μm. The SPP EOMs with this structure have good applicability to optical networks with the ORNoC topology, which effectively solves problems such as those of micro-ring resonators and Mach-Zehnder EOMs when they are used in optical network applications, *i.e.*, poor thermal stability and a low modulation rate.

This work is supported by the National Nature Science Foundation of China under Grant 61561012, in part by the National Nature Science Foundation of China under Grant 61671164, in part by the National Nature Science Foundation of China under Grant 61861012, in part by Guangxi Key Laboratory of Automatic Detecting Technology and Instruments Grant YQ18109, in part by the Guangxi Natural Science Foundation Joint Funding Project 2018GXNSFAA138115 and Guangxi Natural Science Foundation Joint Funding Project 2017GXNSFAA198021. The statements made herein are solely those of the authors.

REFERENCES

1. *Donoho D.L.* Compressed sensing // IEEE Trans. Inf. Theory 2006. V. 52. № 4. P. 1289–1306.
2. *Paczkowski L.W., Balmakhtar M.* Hardware-trusted network-on-chip (NOC) and system-on-chip (SOC) network function virtualization (NFV) data communications // U.S. Patent 10,318,723. Nov. 6, 2019.
3. *Chen K., Li X., Gu H., Song L.* Optical network-on-chip, optical router, and signal transmission method // U.S. Patent Application 10/250,958. Feb. 2, 2019.
4. *Le Beux S., Trajkovic J., O'Connor I., Nicolescu G.* Layout guidelines for 3D architectures including optical ring network-on-chip (ORNoC) // 2011 IEEE/IFIP 19th Internat. Conf. VLSI and System-on-Chip. IEEE. 2011. P. 242–247.
5. *Cerutti I., Acmad M.N.A., Reyes R., Castoldi P., Andriolli N.* Scheduling in multi-wavelength ring-based optical networks-on-chip // J. Opt. Commun. Netw. 2018. V. 10. № 4. P. 322–331.
6. *Wang K., Wang K., Yang Y., Wang Y., Gu H.* Layout optimization methodology for ring-based on-chip optical network // IEICE Electron. Exp. 2019. V. 16. № 20. P. 20190458.
7. *Wang X., Gu H., Yang Y., Wang K., Hao Q.* RPNoC: A ring-based packet-switched optical network-on-chip // IEEE Photonics Technol. Lett. 2015. V. 27. № 4. P. 423–426.
8. *Thelakkat H.M.* Performance and energy evaluation of parallelization strategies for network on chip communication architectures: Case study of canny edge detector application // Diss. Concordia University, 2018.
9. *Hu Y.C., Chen H.M., Zhou H.T.* Mach-Zehnder modulator based on photonic crystal and nanowire waveguide // J. Infrared Millim. Waves. 2018. V. 38. № 4. P. 499–507.
10. *He M., Xu M., Ren Y., Jian J., Ruan Z., Xu Y., Gao S., Sun S., Wen X., Zhou L., Liu L., Guo C., Chen H., Yu S., Liu L., Cai X.* High-performance hybrid silicon and lithium niobate Mach-Zehnder modulators for 100 Gbit s^{-1} and beyond // Nat. Photonics. 2019. V. 13. № 5. P. 359–364.
11. *Yue W.C., Yao P.J., Chen X.L., Tao R.X.* Hybrid dual wedge plasmonic waveguide with long-range propagation and subwavelength mode confinement // J. Infrared Millim. Waves. 2018. V. 37. № 6. P. 663–667.
12. *Badr M.M., Abdelatty M.Y., Swillam M.A.* Ultra-fast silicon electro-optic modulator based on ITO-integrated directional coupler // Phys. Scr. 2019. V. 94. № 6. P. 065502.

13. *Tahersima M.H., Ma Z., Gui Y., Sun S., Wang H., Amin R., Dalir H., Chen R., Miscuglio M., Sorger V.J.* Coupling-enhanced dual ITO layer electro-absorption modulator in silicon photonics // Nanophotonics. 2019. V. 8. № 9. P. 1559–1566.
14. *Kuang Y., Liu Y., Tian L., Han W., Li Z.* A dual-slot electro-optic modulator based on an epsilon-near-zero oxide // IEEE Photonics J. 2019. V. 11. № 4. P. 1–12.
15. *Cooper M.L., Mookherjea S.* Numerically-assisted coupled-mode theory for silicon waveguide couplers and arrayed waveguides // Opt. Exp. 2009. V. 17. № 3. P. 1583–1599.
16. *Bellanca G., Orlandi P., Bassi P.* Assessment of the orthogonal and non-orthogonal coupled-mode theory for parallel optical waveguide couplers // JOSA A. 2018. V. 35. № 4. P. 577–585.
17. *Jin L., Chen Q., Liu W., Song S.* Electro-absorption modulator with dual carrier accumulation layers based on epsilon-near-zero ITO // Plasmonics. 2015. V. 11. № 4. P. 1087–1092.
18. *Kim J.T.* Silicon optical modulators based on tunable plasmonic directional couplers // IEEE J. Sel. Top. Quant. Electron. 2015. V. 21. № 4. P. 184–191.
19. *Kim J.-S., Kim J.T.* Silicon electro-optic modulator based on an ITO-integrated tunable directional coupler // J. Phys. D. Appl. Phys. 2016. V. 49. № 7. P. 075101.
20. *Abdelatty M.Y., Badr M.M., Swillam M.A.* Compact silicon electro-optical modulator using hybrid ITO tri-coupled waveguides // J. Light. Technol. 2018. V. 36. № 18. P. 4198–4204.
21. *Farhan M.S., Zalnezhad E., Bushroa A.R., Sarhan A.A.D.* Electrical and optical properties of indium-tin oxide (ITO) films by ion-assisted deposition (IAD) at room temperature // Int. J. Precis. Eng. Manuf. 2013. V. 14. № 8. P. 1465–1469.
22. *Li Z.-Q., Yue Z., Bai L.D., Liu T.L., Feng D.D., Gu E.D., Li W.C.* Metal ridge-triangular semiconductor of mixed surface plasma waveguide // J. Infrared Millim. Waves. 2017. V. 36. № 6. P. 761–766.
23. FDTD Solutions. Lumerical's Nanophotonic FDTD Simulation Software.
24. *Sun S., Narayana V.K., Sarpkaya I., Crandall J., Soref R.A., Dalir H., El-Ghazawi T., Sorger V.J.* Hybrid photonic-plasmonic nonblocking broadband 5×5 router for optical networks // IEEE Photonics J. 2018. V. 10. № 2. P. 1–12.
25. *Koch U., Hoessbacher C., Niegemann J., Hafner C., Leuthold J.* Digital plasmonic absorption modulator exploiting epsilon-near-zero in transparent conducting oxides // IEEE Photonics J. 2016. V. 8. № 1. P. 1–13.
26. *Kim H.J., Lee S.H., Lee D., Lee A.R., Lim K.-J., Shin W.-S., Kim J.* Improvement of ohmic contact between the indium tin oxide and copper-plated contact of solar cells by using the Cu–Sn alloy film // J. Nanosci. Nanotechnol. 2020. V. 20. № 1. P. 245–251.
27. *Liu E.K., Zhu B.S., Luo J.S.* The physics of semiconductors. Beijing: Electronic Industry Press, 2017.